Journal of
Mechanics of
Materials and Structures

GRADIENT REPRODUCING KERNEL PARTICLE METHOD

Alireza Hashemian and Hossein M. Shodja

Volume 3, Nº 1 January 2008

mathematical sciences publishers

JOURNAL OF MECHANICS OF MATERIALS AND STRUCTURES
Vol. 3, No. 1, 2008

GRADIENT REPRODUCING KERNEL PARTICLE METHOD

ALIREZA HASHEMIAN AND HOSSEIN M. SHODJA

This paper presents an innovative formulation of the RKPM (reproducing kernel particle method) pioneered by Liu. A major weakness of the conventional RKPM is in dealing with the derivative boundary conditions. The EFGM (element free Galerkin method) pioneered by Belytschko shares the same difficulty. The proposed RKPM referred to as GRKPM (gradient RKPM), incorporates the first gradients of the function in the reproducing equation. Therefore in three-dimensional space GRKPM consists of four independent types of shape functions. It is due to this feature that the corrected collocation method can be readily generalized and combined with GRKPM to enforce the EBCs (essential boundary conditions), involving both the field quantity and its first derivatives simultaneously. By considering several plate problems it is observed that GRKPM yields solutions of higher accuracy than those obtained using the conventional approach, while for a desired accuracy the number of particles needed in GRKPM is much less than in the traditional methodology.

1. Introduction

Boundary value problems (BVPs) often have essential boundary conditions (EBCs) that involve derivatives, for example, in beams and plates, where slopes are commonly enforced at the boundaries. Such problems are solved numerically using meshless techniques like the reproducing kernel particle method (RKPM) and the element free Galerkin method (EFGM), pioneered by Liu et al. [1995] and Belytschko et al. [1994b], respectively. However, both methods require an often awkward auxiliary method for enforcing the EBCs. Li and Liu [2002] gives a useful review of the previous methodologies.

We summarize the major contributions specifically aimed at remedying the issue of EBCs. The method of Lagrange multipliers is a classic approach [Belytschko et al. 1994b]. However, it is unattractive because it increases the number of unknowns, causes a loss of positive definiteness, and leads to an awkward system of linear equations. Another method is a modified variational principle [Lu et al. 1994] that interprets the Lagrange multipliers and replaces them by physical quantities. Although it leads to a banded set of equations, the coefficient matrix is not necessarily positive definite and the results are less accurate than those obtained by using Lagrange multipliers. The penalty method [Belytschko et al. 1994a; Zhu and Atluri 1998] is a very simple and effective approach which does not increase the number of unknowns. However, it does not satisfy the EBCs exactly, and its accuracy depends on the penalty factor. Yet another approach couples EFGM and finite element method (FEM) [Krongauz and Belytschko 1996; Liu et al. 1997] by using FEM for the boundaries and their neighboring domains and using EFGM elsewhere. This technique dramatically simplifies enforcing the EBCs. However, it loses the advantage of the meshfree technology near the boundaries. Another idea uses the singular kernel function to enforce the Kronecker delta property [Lancaster and Salkauskas 1981]. It enforces the EBCs

Keywords: meshfree, RKPM, gradient, mixed boundary conditions, plates.

efficiently, but it works only when the dilation parameter falls within a limited range. When it is too large, the convergence rate deteriorates rapidly. Finally, the transformation technique, first proposed by Chen et al. [1996], can efficiently impose the EBCs for meshless methods. However, it cannot be applied when the EBCs involve derivatives.

Liu et al. [1996a] took advantage of the Hermite polynomials and proposed the Hermite reproducing kernel method (HRKM), which incorporates the derivative terms into the reproducing equation. In the one-dimensional formulation, four admissible forms were presented for selecting the modified kernels associated with the derivative terms. However, they claimed that the only form that can be generalized to higher dimensions violates the second order reproducing condition. As a result, it reconstructs the function less accurately than the standard RKPM. Moreover, the EBCs were enforced by an auxiliary method which was not stated explicitly. Atluri et al. [1999] extended the conventional moving least squares (MLS) interpolant, first presented by Lancaster and Salkauskas [1981], to Hermite-type interpolation and called it generalized MLS (GMLS). For illustration, Atluri et al. [1999] considered a one-dimensional thin beam and imposed the EBC using the penalty method. Later, Tiago and Leitão [2004] used GMLS to solve the isotropic Kirchhoff plate. They enforced the EBCs using Lagrange multipliers. Li et al. [2003] and Lam et al. [2006] employed the Hermite theorem to construct the Hermite–Cloud method based on the classical RKPM but used a fixed kernel instead of a moving one. They chose the strong form of governing partial differential equations; that is, they used the point collocation technique to discretize the governing partial differential equations. Liu et al. [2004] combined a meshfree and a finite element interpolant by introducing a hybrid fundamental equation that incorporates the concepts of both RKPM and FEM. In this manner, they generated a class of hybrid interpolation functions that may achieve a higher order of smoothness in multiple dimensions. They called this technology the reproducing kernel element method (RKEM) and pointed out that it has a great advantage over the traditional FEM. Li et al. [2004] proposed that, by extending the RKEM interpolant to a Hermite-type interpolant, one can obtain higher order Kronecker delta properties suitable for solving BVPs involving higher order partial differential equations. It should be emphasized that RKEM is a mesh-based technique which requires element defining and mapping.

In 1999, we were working on a Master's thesis that studied solving beam-column problems by meshless methods, particularly RKPM. During our work, we found it difficult to enforce the EBCs associated with the deflection and rotation of beam-columns. As the work progressed, we realized that the usual transformation method, however efficient, cannot apply to the derivative type of EBCs. We generalized the transformation technique so that it could accommodate not only the function but also the derivative type of EBCs. In so doing, we modified the RKPM formulation extensively and successfully linked it to the generalized transformation technique. We added a gradient term to the reproducing equation, and, for this reason, we called the new approach the gradient RKPM (GRKPM). The advantage of GRKPM over RKPM is that, in addition to exactly enforcing the EBCs without resorting to the penalty method or Lagrange multipliers, it gives more accurate results and converges faster. Moreover, it gives a banded set of equations with a positive definite matrix [Hashemian 2000].

The one-dimensional formulation of GRKPM of [Hashemian 2000] is not extended straightforwardly to multiple dimensions. In three dimensions, a major difficulty is in choosing the correction functions to produce a well-conditioned system. However, once that has been done, the formulation can be reduced easily back to one or two dimensions. In this work, we present GRKPM in three dimensions, and

hence one and two as well. Besides affirming its accuracy and good convergence, we establish that the approach enforces mixed EBCs by reexamining several thin plate problems solved previously by other methods. Next, we further demonstrate the method's efficacy by considering more complex and physically important problems that are poorly solved by the existing meshless techniques (RKPM and EFGM).

2. Formulating the GRKPM

2.1. ***Reproducing equation.*** The starting point for the conventional RKPM is that a given function $u(\boldsymbol{x})$ in the three-dimensional space (with coordinates x_k) can be expressed by the reproducing formula

$$u^R(\boldsymbol{x}) = \int_\Omega \bar{\phi}_a^0(\boldsymbol{x}; \boldsymbol{x}-\boldsymbol{y}) u(\boldsymbol{y}) d\Omega,$$

where $u^R(\boldsymbol{x})$ is the reproduced function, a is a dilation parameter, and $\bar{\phi}_a^0(\boldsymbol{x}; \boldsymbol{x}-\boldsymbol{y})$ is the modified kernel function associated with the function. We propose expressing $u^R(\boldsymbol{x})$ as

$$u^R(\boldsymbol{x}) = \int_\Omega \bar{\phi}_a^0(\boldsymbol{x}; \boldsymbol{x}-\boldsymbol{y}) u(\boldsymbol{y}) d\Omega + \sum_{k=1}^{3} \int_\Omega \bar{\phi}_a^k(\boldsymbol{x}; \boldsymbol{x}-\boldsymbol{y}) u_{,k}(\boldsymbol{y}) d\Omega. \tag{1}$$

In Equation (1), $u_{,k}(\boldsymbol{y}) = \partial u(\boldsymbol{y})/\partial y_k$ and $\bar{\phi}_a^k(\boldsymbol{x}; \boldsymbol{x}-\boldsymbol{y})$ for $k \neq 0$ is the modified kernel function associated with $u_{,k}(\boldsymbol{y})$. For $k = 0, 1, 2, 3$, we define

$$\bar{\phi}_a^k(\boldsymbol{x}; \boldsymbol{x}-\boldsymbol{y}) = C^k(\boldsymbol{x}; \boldsymbol{x}-\boldsymbol{y}) \phi_a(\boldsymbol{x}-\boldsymbol{y}),$$

where $\phi_a(\boldsymbol{x}-\boldsymbol{y})$ is the kernel function and $C^k(\boldsymbol{x}; \boldsymbol{x}-\boldsymbol{y})$ are correction functions, which are derived from a reference function

$$C(\boldsymbol{x}; \boldsymbol{x}-\boldsymbol{y}) = b_0(\boldsymbol{x}) + \sum_{i=1}^{3} b_i(\boldsymbol{x})(x_i - y_i) + \frac{1}{2} \sum_{i=1}^{3} \sum_{j=1}^{3} b_{ij}(\boldsymbol{x})(x_i - y_i)(x_j - y_j),$$

by the relations

$$\begin{aligned} C^0(\boldsymbol{x}; \boldsymbol{x}-\boldsymbol{y}) &= b_0(\boldsymbol{x}) + \sum_{i=1}^{3} b_i(\boldsymbol{x})(x_i - y_i), \\ C^k(\boldsymbol{x}; \boldsymbol{x}-\boldsymbol{y}) &= -\frac{\partial C(\boldsymbol{x}; \boldsymbol{x}-\boldsymbol{y})}{\partial y_k}, \quad k = 1, 2, 3. \end{aligned} \tag{2}$$

In the reference function, b_i and b_{ij} ($b_{ij} = b_{ji}$) are unknown coefficients to be determined by the completeness conditions. It should be noted that $C^0(\boldsymbol{x}; \boldsymbol{x}-\boldsymbol{y})$ is just the part of $C(\boldsymbol{x}; \boldsymbol{x}-\boldsymbol{y})$ affine in $\boldsymbol{y}$.

Using the previous three equations, one obtains

$$\bar{\phi}_a^0(\boldsymbol{x};\boldsymbol{x}-\boldsymbol{y}) = \left[b_0(\boldsymbol{x}) + \sum_{i=1}^{3} b_i(\boldsymbol{x})(x_i - y_i)\right]\phi_a(\boldsymbol{x}-\boldsymbol{y}),$$
$$\bar{\phi}_a^k(\boldsymbol{x};\boldsymbol{x}-\boldsymbol{y}) = \left[b_k(\boldsymbol{x}) + \sum_{i=1}^{3} b_{ki}(\boldsymbol{x})(x_i - y_i)\right]\phi_a(\boldsymbol{x}-\boldsymbol{y}), \quad k = 1, 2, 3.$$

In this result, note that the forms chosen in Equation (2) for the correction functions assure the linear independence of the modified kernels.

2.2. ***Completeness.*** Consider the Taylor's series of $u(\boldsymbol{y})$ around point $\boldsymbol{x}$ up to second order:

$$u(\boldsymbol{y}) \cong u(\boldsymbol{x}) - \sum_{i=1}^{3}(x_i - y_i)u_{,i}(\boldsymbol{x}) + \frac{1}{2}\sum_{i=1}^{3}\sum_{j=1}^{3}(x_i - y_i)(x_j - y_j)u_{,ij}(\boldsymbol{x}),$$

Upon substituting this into Equation (1), it follows that

$$u^R(\boldsymbol{x}) = u(\boldsymbol{x})R_0(\boldsymbol{x}) - \sum_{m=1}^{3} u_{,m}(\boldsymbol{x})R_m(\boldsymbol{x}) + \frac{1}{2}\sum_{m=1}^{3}\sum_{n=1}^{3} u_{,mn}(\boldsymbol{x})R_{mn}(\boldsymbol{x}) + \text{Err}, \tag{4}$$

where Err denotes the cumulative truncation error and

$$R_0(\boldsymbol{x}) = \int_\Omega \bar{\phi}_a^0(\boldsymbol{x}-\boldsymbol{y})d\Omega,$$
$$R_m(\boldsymbol{x}) = \int_\Omega (x_m - y_m)\bar{\phi}_a^0(\boldsymbol{x}-\boldsymbol{y})d\Omega - \int_\Omega \bar{\phi}_a^m(\boldsymbol{x}-\boldsymbol{y})d\Omega, \quad m = 1, 2, 3,$$
$$R_{mn}(\boldsymbol{x}) = R_{nm}(\boldsymbol{x}) = \int_\Omega (x_m - y_m)(x_n - y_n)\bar{\phi}_a^0(\boldsymbol{x}-\boldsymbol{y})d\Omega$$
$$- \int_\Omega (x_m - y_m)\bar{\phi}_a^n(\boldsymbol{x}-\boldsymbol{y})d\Omega - \int_\Omega (x_n - y_n)\bar{\phi}_a^m(\boldsymbol{x}-\boldsymbol{y})d\Omega, \quad m, n = 1, 2, 3.$$

In view of Equation (4), the completeness condition on $u^R(\boldsymbol{x})$ leads to 10 independent conditions [Liu et al. 1996b; Liu et al. 1996a]. Introducing the ijkth moment at the point $\boldsymbol{x}$ with respect to the kernel function $\phi_a(\boldsymbol{x}-\boldsymbol{y})$ as

$$m_{ijk}(\boldsymbol{x}) = \int_\Omega (x_1 - y_1)^i (x_2 - y_2)^j (x_3 - y_3)^k \phi_a(\boldsymbol{x}-\boldsymbol{y})d\Omega, \tag{5}$$

it follows that

$$\boldsymbol{M}(\boldsymbol{x})\boldsymbol{\beta}(\boldsymbol{x}) = \boldsymbol{H}, \tag{6}$$

in which $\boldsymbol{M}(\boldsymbol{x})$ is

$$\begin{bmatrix}
m_{000} & m_{100} & m_{010} & m_{001} & 0 & 0 & 0 & 0 & 0 & 0 \\
m_{100} & m_{200}-m_{000} & m_{110} & m_{101} & -m_{100} & -m_{010} & -m_{001} & 0 & 0 & 0 \\
m_{010} & m_{110} & m_{020}-m_{000} & m_{011} & 0 & -m_{100} & 0 & -m_{010} & -m_{001} & 0 \\
m_{001} & m_{101} & m_{011} & m_{002}-m_{000} & 0 & 0 & -m_{100} & 0 & -m_{010} & -m_{001} \\
m_{200} & m_{300}-2m_{100} & m_{210} & m_{201} & -2m_{200} & -2m_{110} & -2m_{101} & 0 & 0 & 0 \\
m_{110} & m_{210}-m_{010} & m_{120}-m_{100} & m_{111} & -m_{110} & -m_{020}-m_{200} & -m_{011} & -m_{110} & -m_{101} & 0 \\
m_{101} & m_{201}-m_{001} & m_{111} & m_{102}-m_{100} & -m_{101} & -m_{011} & -m_{200}-m_{002} & 0 & -m_{110} & -m_{101} \\
m_{020} & m_{120} & m_{030}-2m_{010} & m_{021} & 0 & -2m_{110} & 0 & -2m_{020} & -2m_{011} & 0 \\
m_{011} & m_{111}-m_{001} & m_{021} & m_{012}-m_{010} & 0 & -m_{101} & -m_{110} & -m_{011} & -m_{020}-m_{002} & -m_{011} \\
m_{002} & m_{102} & m_{012} & m_{003}-2m_{001} & 0 & 0 & -2m_{101} & 0 & -2m_{011} & -2m_{002}
\end{bmatrix},$$

the vector containing the unknown coefficients

$$\boldsymbol{\beta}^T(\boldsymbol{x}) = \begin{bmatrix} b_0(\boldsymbol{x}) & b_1(\boldsymbol{x}) & b_2(\boldsymbol{x}) & b_3(\boldsymbol{x}) & b_{11}(\boldsymbol{x}) & b_{12}(\boldsymbol{x}) & b_{13}(\boldsymbol{x}) & b_{22}(\boldsymbol{x}) & b_{23}(\boldsymbol{x}) & b_{33}(\boldsymbol{x}) \end{bmatrix},$$

and

$$\boldsymbol{H}^T = \begin{bmatrix} 1 & 0 & 0 & 0 & 0 & 0 & 0 & 0 & 0 & 0 \end{bmatrix}.$$

The unknown b_i and b_{ij} are readily determined by solving Equation (6). We compute the first derivatives of $\boldsymbol{\beta}(\boldsymbol{x})$ by differentiating Equation (6)

$$\boldsymbol{M}(\boldsymbol{x})\boldsymbol{\beta}_{,m}(\boldsymbol{x}) = -\boldsymbol{M}_{,m}(\boldsymbol{x})\boldsymbol{\beta}(\boldsymbol{x}), \quad m = 1, 2, 3,$$

and compute the second derivatives by differentiating the above, as

$$\begin{aligned}
\boldsymbol{M}(\boldsymbol{x})\boldsymbol{\beta}_{,mn}(\boldsymbol{x}) = &-\boldsymbol{M}_{,mn}(\boldsymbol{x})\boldsymbol{\beta}(\boldsymbol{x}) \\
&- \boldsymbol{M}_{,m}(\boldsymbol{x})\boldsymbol{\beta}_{,n}(\boldsymbol{x}) \\
&- \boldsymbol{M}_{,n}(\boldsymbol{x})\boldsymbol{\beta}_{,m}(\boldsymbol{x}), \quad m, n = 1, 2, 3,
\end{aligned}$$

in the order shown above.

2.3. ***Shape functions.*** To extract the shape functions and their associated derivatives, one must discretize the integral in Equation (1). In this paper, we use the trapezoidal rule, and the equation becomes

$$u^R(\boldsymbol{x}) = \sum_{i=1}^{\mathrm{NP}} \psi_i^0(\boldsymbol{x}) u^i + \sum_{k=1}^{3} \sum_{i=1}^{\mathrm{NP}} \psi_i^k(\boldsymbol{x}) u^i_{,k}, \tag{7}$$

where NP is the number of particles,[1] $u^i = u(\boldsymbol{y}^i)$, $u^i_{,k} = \partial u(\boldsymbol{y})/\partial y_k|_{\boldsymbol{y}=\boldsymbol{y}^i}$, and

$$\begin{aligned}
\psi_i^0(\boldsymbol{x}) &= \left[b_0(\boldsymbol{x}) + \sum_{j=1}^{3} b_j(\boldsymbol{x})(x_j - y_j^i) \right] \phi_a(\boldsymbol{x} - \boldsymbol{y}^i) \Delta \boldsymbol{y}^i, \\
\psi_i^k(\boldsymbol{x}) &= \left[b_k(\boldsymbol{x}) + \sum_{j=1}^{3} b_{kj}(\boldsymbol{x})(x_j - y_j^i) \right] \phi_a(\boldsymbol{x} - \boldsymbol{y}^i) \Delta \boldsymbol{y}^i,
\end{aligned} \tag{8}$$

[1] Smooth particle hydrodynamics (SPH) is a meshfree method which was first proposed by Lucy [1977]. Utilizing this method, he modeled the collective behavior of a discrete set of physical particles in astrophysics. For this reason, in RKPM [Liu et al. 1995] and in the present work, the y^i are called particles rather than nodes.

in which $\psi_i^k(\boldsymbol{x})$ is the kth shape function for the ith particle evaluated at $\boldsymbol{x}$, and $\Delta \boldsymbol{y}^i$ is the area belonging to the ith particle.

Many authors, for example Donning and Liu [1998] and Liu [2003], have extensively studied various window functions and their effects. In the present work, we use the cubic spline

$$\phi(z) = \begin{cases} \dfrac{2}{3} - 4z^2 + 4z^3, & 0 \le |z| \le \dfrac{1}{2}, \\ \dfrac{4}{3} - 4z + 4z^2 - \dfrac{4}{3}z^3, & \dfrac{1}{2} < |z| \le 1, \\ 0, & \text{otherwise}, \end{cases}$$

and construct the three-dimensional window function by multiplying the one-dimensional window functions:

$$\phi_a(\boldsymbol{x} - \boldsymbol{y}) = \prod_{i=1}^{3} \frac{1}{a_i} \phi\left(\frac{x_i - y_i}{a_i}\right),$$

in which a_i is the dilation parameter associated with the x_i-direction.

Numerically evaluating the unknowns b_i, b_{ij}, and their derivatives requires discretizing the integral in Equation (5) and subsequently calculating the moment $m_{ijk}(\boldsymbol{x})$. To satisfy the consistency condition, the technique used for discretizing the reproducing equation must be used also for the moment equation [Chen et al. 1996].

The first derivatives of the shape functions are obtained by differentiating Equation (8):

$$\begin{aligned} \left[\psi_i^0(\boldsymbol{x})\right]_{,m} = &\left\{ [b_0(\boldsymbol{x})]_{,m} + \sum_{j=1}^{3} [b_j(\boldsymbol{x})]_{,m} (x_j - y_j^i) + b_m(\boldsymbol{x}) \right\} \phi_a(\boldsymbol{x} - \boldsymbol{y}^i) \Delta \boldsymbol{y}^i \\ &+ \left\{ b_0(\boldsymbol{x}) + \sum_{j=1}^{3} b_j(\boldsymbol{x})(x_j - y_j^i) \right\} \left[\phi_a(\boldsymbol{x} - \boldsymbol{y}^i)\right]_{,m} \Delta \boldsymbol{y}^i, \end{aligned}$$

$$\begin{aligned} \left[\psi_i^k(\boldsymbol{x})\right]_{,m} = &\left\{ \left[b_k(\boldsymbol{x})\right]_{,m} + \sum_{j=1}^{3} [b_{kj}(\boldsymbol{x})]_{,m} (x_j - y_j^i) + b_{km}(\boldsymbol{x}) \right\} \phi_a(\boldsymbol{x} - \boldsymbol{y}^i) \Delta \boldsymbol{y}^i \\ &+ \left\{ b_k(\boldsymbol{x}) + \sum_{j=1}^{3} b_{kj}(\boldsymbol{x})(x_j - y_j^i) \right\} \left[\phi_a(\boldsymbol{x} - \boldsymbol{y}^i)\right]_{,m} \Delta \boldsymbol{y}^i, \quad k = 1, 2, 3, \end{aligned}$$

with $i = 1, 2, \ldots,$ NP and $m = 1, 2, 3$. Differentiating again leads to the shape functions' second derivatives:

$$\begin{aligned}
\left[\psi_i^0(\boldsymbol{x})\right]_{,mn} = &\left\{[b_0(\boldsymbol{x})]_{,mn} + \sum_{j=1}^{3}[b_j(\boldsymbol{x})]_{,mn}(x_j - y_j^i) + [b_n(\boldsymbol{x})]_{,m} + [b_m(\boldsymbol{x})]_{,n}\right\}\phi_a(\boldsymbol{x} - \boldsymbol{y}^i)\Delta\boldsymbol{y}^i \\
&+ \left\{[b_0(\boldsymbol{x})]_{,n} + \sum_{J=1}^{3}[b_j(\boldsymbol{x})]_{,n}(x_j - y_j^i) + b_n(\boldsymbol{x})\right\}[\phi_a(\boldsymbol{x} - \boldsymbol{y}^i)]_{,m}\Delta\boldsymbol{y}^i \\
&+ \left\{[b_0(\boldsymbol{x})]_{,m} + \sum_{j=1}^{3}[b_j(\boldsymbol{x})]_{,m}(x_j - y_j^i) + b_m(\boldsymbol{x})\right\}[\phi_a(\boldsymbol{x} - \boldsymbol{y}^i)]_{,n}\Delta\boldsymbol{y}^i \\
&+ \left\{b_0(\boldsymbol{x}) + \sum_{j=1}^{3}b_j(\boldsymbol{x})(x_j - y_j^i)\right\}[\phi_a(\boldsymbol{x} - \boldsymbol{y}^i)]_{,mn}\Delta\boldsymbol{y}^i,
\end{aligned}$$

$$\begin{aligned}
\left[\psi_i^k(\boldsymbol{x})\right]_{,mn} = &\left\{[b_k(\boldsymbol{x})]_{,mn} + \sum_{j=1}^{3}[b_{kj}(\boldsymbol{x})]_{,mn}(x_j - y_j^i) + [b_{kn}(\boldsymbol{x})]_{,m} + [b_{km}(\boldsymbol{x})]_{,n}\right\}\phi_a(\boldsymbol{x} - \boldsymbol{y}^i)\Delta\boldsymbol{y}^i \\
&+ \left\{[b_k(\boldsymbol{x})]_{,n} + \sum_{j=1}^{3}[b_{kj}(\boldsymbol{x})]_{,n}(x_j - y_j^i) + b_{kn}(\boldsymbol{x})\right\}[\phi_a(\boldsymbol{x} - \boldsymbol{y}^i)]_{,m}\Delta\boldsymbol{y}^i \\
&+ \left\{[b_k(\boldsymbol{x})]_{,m} + \sum_{j=1}^{3}[b_{kj}(\boldsymbol{x})]_{,m}(x_j - y_j^i) + b_{km}(\boldsymbol{x})\right\}[\phi_a(\boldsymbol{x} - \boldsymbol{y}^i)]_{,n}\Delta\boldsymbol{y}^i \\
&+ \left\{b_k(\boldsymbol{x}) + \sum_{j=1}^{3}b_{kj}(\boldsymbol{x})(x_j - y_j^i)\right\}[\phi_a(\boldsymbol{x} - \boldsymbol{y}^i)]_{,mn}\Delta\boldsymbol{y}^i, \quad k = 1, 2, 3,
\end{aligned}$$

with $i = 1, 2, \ldots,$ NP and $m, n = 1, 2, 3$.

3. Presenting the shape functions: departure from the conventional type

The aim of this section is to present the shape functions that follow from the proposed reproducing equation, and for this purpose we consider two-dimensional shape functions.

In two dimensions, Equation (8) yields three different types of shape functions $\psi_i^0(\boldsymbol{x})$, $\psi_i^1(\boldsymbol{x})$ and $\psi_i^2(\boldsymbol{x})$:

$$\begin{aligned}
\psi_i^0(\boldsymbol{x}) &= \left[b_0(\boldsymbol{x}) + \sum_{j=1}^{2}b_j(\boldsymbol{x})(x_j - y_j^i)\right]\phi_a(\boldsymbol{x} - \boldsymbol{y}^i)\Delta\boldsymbol{y}^i, \\
\psi_i^k(\boldsymbol{x}) &= \left[b_k(\boldsymbol{x}) + \sum_{j=1}^{2}b_{kj}(\boldsymbol{x})(x_j - y_j^i)\right]\phi_a(\boldsymbol{x} - \boldsymbol{y}^i)\Delta\boldsymbol{y}^i, \quad k = 1, 2,
\end{aligned}$$

with $i = 1, 2, \ldots,$ NP. We emphasize that the conventional RKPM has only one shape function $\psi_i(\boldsymbol{x})$, regardless of the dimension of the problem, whereas the present method gives rise to k additional shape functions, $\psi_i^k(\boldsymbol{x})$, for k-dimensional Euclidean space.

Figure 1 shows the shape functions for the conventional RKPM, and Figures 2 and 3 depict the shape functions corresponding to GRKPM. In these figures, the region $[0, 5]^2$ contains 11×11 uniformly distributed particles. The dilation parameter is chosen to be twice the particle spacing in each direction. For illustration, Figures 1–3 display the shape functions associated with certain particles. Specifically selected are the corners located at $(0, 0)$, $(5, 0)$, $(5, 5)$, and $(0, 5)$; the mid-edge points $(2.5, 0)$, $(5, 2.5)$, $(2.5, 5)$, and $(0, 2.5)$; and the center $(2.5, 2.5)$. From Figures 1 and 2, the $\psi_i^0(\boldsymbol{x})$ from GRKPM are, modulo amplitude, the same as the $\psi_i(\boldsymbol{x})$ from RKPM. Comparing within Figure 3 reveals that the $\psi_i^2(\boldsymbol{x})$ are simply the $\psi_i^1(\boldsymbol{x})$ rotated 90° counterclockwise about the region's center. We point out that $\psi_i^1(\boldsymbol{x})$ and $\psi_i^2(\boldsymbol{x})$ are the shape functions associated with the first derivative of the function in the x_1 and x_2-direction.

4. Applying essential boundary conditions

In the meshfree methods (RKPM/EFGM), enforcing EBCs has been a controversial issue among investigators. The basic shortcoming of the methods is that the shape functions do not possess the Kronecker delta property. For this reason, enforcing the EBCs is not as convenient as in FEM.

4.1. ***Statement of the problem.*** Consider a three-dimensional domain Ω with the boundary Γ and the associated BVP

$$Lu(\boldsymbol{x}) = f(\boldsymbol{x}), \quad \boldsymbol{x} \in \Omega, \tag{9}$$

in which L is a linear differential operator. Natural boundary conditions may have arbitrary form, whereas EBCs may prescribe the field quantity and/or its first derivatives

$$u_{,k}(\boldsymbol{x}) = g_k(\boldsymbol{x}), \qquad \boldsymbol{x} \in \Gamma_{\text{eb}}^k, \quad k = 0, 1, 2, 3, \tag{10}$$

where Γ_{eb}^0 and Γ_{eb}^k are the set of all points $\boldsymbol{x}$ at which $u(\boldsymbol{x})$ and $u_{,k}(\boldsymbol{x})$ are prescribed. Thus the essential boundary is

$$\Gamma_{\text{eb}} = \bigcup_{k=0}^{3} \Gamma_{\text{eb}}^k.$$

It is interesting to note that $\Gamma_{\text{eb}}^i \cap \Gamma_{\text{eb}}^j$ may not be empty for $i \neq j$. Suppose S is the space of all $H_2^{(2)}(\Omega)$ functions that satisfy the boundary conditions (10), and define V to be the space of all $H_2^{(2)}(\Omega)$ functions that satisfy the homogeneous EBCs. The spaces S and V may be expressed as

$$S \equiv \left\{ u \mid u \in H_2^{(2)}(\Omega),\, u_{,k}(\boldsymbol{x}) = g_k(\boldsymbol{x}) \text{ on } \Gamma_{\text{eb}}^k, \quad k = 0, 1, 2, 3 \right\}, \tag{11a}$$

$$V \equiv \left\{ w \mid w \in H_2^{(2)}(\Omega),\, w_{,k}(\boldsymbol{x}) = 0 \text{ on } \Gamma_{\text{eb}}^k, \quad k = 0, 1, 2, 3 \right\}, \tag{11b}$$

where $H_2^{(2)}(\Omega)$ is a Sobolev space. The governing Equation (9) is cast into the weak form

$$\int_\Omega w(\boldsymbol{x})[Lu(\boldsymbol{x}) - f(\boldsymbol{x})]^2 d\Omega = 0. \tag{12}$$

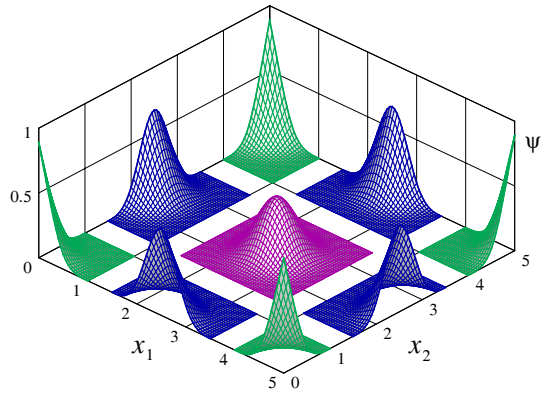

Figure 1. Conventional RKPM shape functions plotted at the corners, mid-edges, and center of the 11×11 uniformly distributed particles with dilation parameter $\boldsymbol{a} = 2\Delta \boldsymbol{y}$.

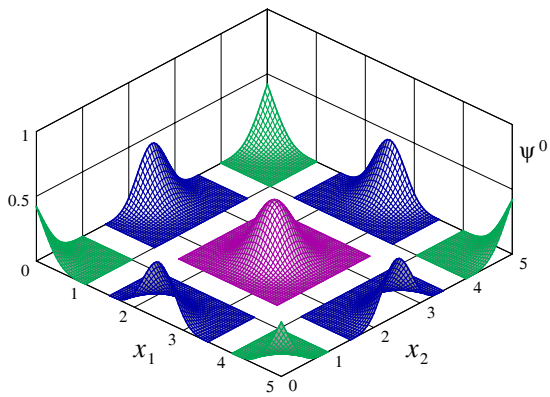

Figure 2. The first type of GRKPM shape functions plotted at the corners, mid-edges, and center of the 11×11 uniformly distributed particles with dilation parameter $\boldsymbol{a} = 2\Delta \boldsymbol{y}$.

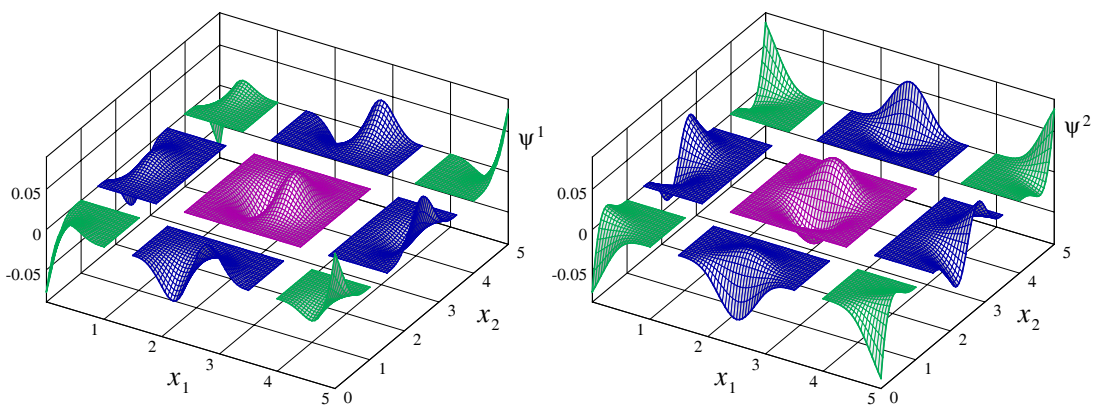

Figure 3. The second and third types of GRKPM shape functions plotted at the corners, mid-edges, and center of the 11×11 uniformly distributed particles with dilation parameter $\boldsymbol{a} = 2\Delta \boldsymbol{y}$.

Employing the shape functions developed in Section 2.3, $u^R(\boldsymbol{x})$ and $w^R(\boldsymbol{x})$ may be written as

$$u^R(\boldsymbol{x}) = \boldsymbol{\psi}(\boldsymbol{x})\boldsymbol{d}, \tag{13a}$$

$$w^R(\boldsymbol{x}) = \boldsymbol{\psi}(\boldsymbol{x})\boldsymbol{c}, \tag{13b}$$

with

$$\boldsymbol{\psi}(\boldsymbol{x}) = \left[\boldsymbol{\psi}_1(\boldsymbol{x}) \;\; \boldsymbol{\psi}_2(\boldsymbol{x}) \;\; \cdots \;\; \boldsymbol{\psi}_{\mathrm{NP}}(\boldsymbol{x})\right], \tag{14a}$$

$$\boldsymbol{\psi}_i(\boldsymbol{x}) = \left[\psi_i^0(\boldsymbol{x}) \;\; \psi_i^1(\boldsymbol{x}) \;\; \psi_i^2(\boldsymbol{x}) \;\; \psi_i^3(\boldsymbol{x})\right], \tag{14b}$$

where $\psi_i^k(\boldsymbol{x}),\ k = 0, 1, 2, 3$ is given by Equation (8). The vector $\boldsymbol{d}$ contains the unknowns associated with the degrees of freedom (DOF) u and $u_{,k}$, $k = 1, 2, 3$. We prefer to represent $\boldsymbol{d}$ as

$$\boldsymbol{d} = \left[\boldsymbol{d}_1{}^T \;\; \boldsymbol{d}_2{}^T \;\; \cdots \;\; \boldsymbol{d}_{\mathrm{NP}}{}^T\right], \tag{15a}$$

$$\boldsymbol{d}_i{}^T = \left[d_i^0 \;\; d_i^1 \;\; d_i^2 \;\; d_i^3\right]. \tag{15b}$$

The unknown vector $\boldsymbol{c}$ pertains to the test function $w^R(\boldsymbol{x})$, which we arrange to have the same structure as $\boldsymbol{d}$. In view of Equations (13)–(15), Equation (12) may be written as

$$\boldsymbol{c}^T\boldsymbol{r} = 0, \tag{16}$$

where

$$\boldsymbol{r} = \boldsymbol{K}\boldsymbol{d} - \boldsymbol{f}, \qquad \boldsymbol{K} = \int_\Omega \boldsymbol{\psi}^T(\boldsymbol{x}) L \boldsymbol{\psi}(\boldsymbol{x}) d\Omega, \qquad \boldsymbol{f} = \int_\Omega \boldsymbol{\psi}^T(\boldsymbol{x}) f(\boldsymbol{x}) d\Omega.$$

The matrix $\boldsymbol{K}$ depends on the operator L. In the next section, we show that the set problem (16) can be rigorously solved for $\boldsymbol{d}$ by extending the corrected collocation method.

4.2. ***Extending the corrected collocation method to GRKPM.*** In collocation methods, the EBCs are enforced exactly at the boundary particles. A number of collocation methods have been developed. The traditional collocation methods, including direct [Lu et al. 1994] and modified [Zhu and Atluri 1998], lead to some inconsistencies when applied to the conventional RKPM [Wagner and Liu 2000]. These inconsistencies exist because the conventional RKPM's shape functions do not possess the Kronecker delta property. Wagner and Liu [2000] give a remedy. Their work is based on the transformation technique [Chen et al. 1996] and is limited to enforcing the EBCs for the function itself. Moreover, the conventional RKPM deals with only one type of shape function. Therefore, in the present situation, where the EBCs involve the function and/or its first derivatives and there are four types of shape functions, the collocation given in [Wagner and Liu 2000] is not applicable and must be modified appropriately.

The starting point is to partition each of the vectors $\boldsymbol{d}$, $\boldsymbol{c}$, and $\boldsymbol{r}$ into two subvectors

$$\boldsymbol{r} = \begin{bmatrix} \boldsymbol{r}_{\mathrm{eb}} \\ \boldsymbol{r}_{\sim\mathrm{eb}} \end{bmatrix}, \qquad \boldsymbol{c} = \begin{bmatrix} \boldsymbol{c}_{\mathrm{eb}} \\ \boldsymbol{c}_{\sim\mathrm{eb}} \end{bmatrix}, \qquad \boldsymbol{d} = \begin{bmatrix} \boldsymbol{d}_{\mathrm{eb}} \\ \boldsymbol{d}_{\sim\mathrm{eb}} \end{bmatrix}. \tag{17}$$

The subscript eb labels the n_{eb} parameters that pertain to the EBCs of Equation (10), whereas $\sim$eb labels the remaining $n_{\sim\mathrm{eb}}$ parameters. (Hence $n_{\mathrm{eb}} + n_{\sim\mathrm{eb}}$ counts the total DOF of the system.) Note that each

particle is allowed to have four DOF in u and $u_{,k}$, $k = 1, 2, 3$. Once the shape function $\boldsymbol{\psi}(\boldsymbol{x})$ in Equation (14a) and its first derivatives are evaluated for the ith particle $\boldsymbol{x}^i$, we may define the matrix

$$\hat{\boldsymbol{\psi}}^T(\boldsymbol{x}^i) = \left[\boldsymbol{\psi}^T(\boldsymbol{x}^i) \;\; \boldsymbol{\psi}_{,1}^T(\boldsymbol{x}^i) \;\; \boldsymbol{\psi}_{,2}^T(\boldsymbol{x}^i) \;\; \boldsymbol{\psi}_{,3}^T(\boldsymbol{x}^i)\right].$$

The square matrix containing the shape functions and their derivatives for a system with NP particles may written as

$$\hat{\boldsymbol{\Psi}}^T = \left[\hat{\boldsymbol{\psi}}^T(\boldsymbol{x}^1) \;\; \hat{\boldsymbol{\psi}}^T(\boldsymbol{x}^2) \;\; \cdots \;\; \hat{\boldsymbol{\psi}}^T(\boldsymbol{x}^{\mathrm{NP}})\right]. \tag{18}$$

Defining

$$\hat{\boldsymbol{u}}^T(\boldsymbol{x}^i) = \left[u(\boldsymbol{x}^i) \;\; u_{,1}(\boldsymbol{x}^i) \;\; u_{,2}(\boldsymbol{x}^i) \;\; u_{,3}(\boldsymbol{x}^i)\right],$$

we replace Equation (13a) by

$$\hat{\boldsymbol{u}}(\boldsymbol{x}^i) = \hat{\boldsymbol{\psi}}(\boldsymbol{x}^i)\boldsymbol{d},$$

and, with the aid of Equation (18), we have

$$\hat{\boldsymbol{U}} = \hat{\boldsymbol{\Psi}}\boldsymbol{d}, \tag{19}$$

where

$$\hat{\boldsymbol{U}}^T = \left[\hat{\boldsymbol{u}}^T(\boldsymbol{x}^1) \;\; \hat{\boldsymbol{u}}^T(\boldsymbol{x}^2) \;\; \cdots \;\; \hat{\boldsymbol{u}}^T(\boldsymbol{x}^{\mathrm{NP}})\right].$$

Next, we define the vector

$$\hat{\boldsymbol{W}}^T = \left[\hat{\boldsymbol{w}}^T(\boldsymbol{x}^1) \;\; \hat{\boldsymbol{w}}^T(\boldsymbol{x}^2) \;\; \cdots \;\; \hat{\boldsymbol{w}}^T(\boldsymbol{x}^{\mathrm{NP}})\right],$$

where

$$\hat{\boldsymbol{w}}^T(\boldsymbol{x}^i) = \left[w(\boldsymbol{x}^i) \;\; w_{,1}(\boldsymbol{x}^i) \;\; w_{,2}(\boldsymbol{x}^i) \;\; w_{,3}(\boldsymbol{x}^i)\right],$$

so that, from Equation (18), we have

$$\hat{\boldsymbol{W}} = \hat{\boldsymbol{\Psi}}\boldsymbol{c}. \tag{20}$$

Repeating for the vectors $\hat{\boldsymbol{W}}$ and $\boldsymbol{c}$ the partition scheme in Equation (17), Equation (20) takes the form

$$\begin{bmatrix} \hat{\boldsymbol{W}}_{\mathrm{eb}} \\ \hat{\boldsymbol{W}}_{\sim\mathrm{eb}} \end{bmatrix} = \begin{bmatrix} \hat{\boldsymbol{E}} & \hat{\boldsymbol{F}} \\ \hat{\boldsymbol{G}} & \hat{\boldsymbol{H}} \end{bmatrix} \begin{bmatrix} \boldsymbol{c}_{\mathrm{eb}} \\ \boldsymbol{c}_{\sim\mathrm{eb}} \end{bmatrix}. \tag{21}$$

This, in conjunction with Equation (11b), implies that $\hat{\boldsymbol{W}}_{\mathrm{eb}} = \boldsymbol{0}$ and $\hat{\boldsymbol{W}}_{\sim\mathrm{eb}}$ is arbitrary, hence

$$\begin{bmatrix} \hat{\boldsymbol{E}} & \hat{\boldsymbol{F}} \end{bmatrix} \begin{bmatrix} \boldsymbol{c}_{\mathrm{eb}} \\ \boldsymbol{c}_{\sim\mathrm{eb}} \end{bmatrix} = \boldsymbol{0},$$

and $\boldsymbol{c}_{\sim\mathrm{eb}}$ is arbitrary.

Let

$$\boldsymbol{T} = \begin{bmatrix} \hat{\boldsymbol{E}} & \hat{\boldsymbol{F}} \\ \boldsymbol{0} & \boldsymbol{I} \end{bmatrix}, \qquad \text{and} \qquad \bar{\boldsymbol{c}} = \boldsymbol{T}\boldsymbol{c},$$

then

$$\bar{\boldsymbol{c}}_{\mathrm{eb}} = \boldsymbol{0}, \tag{22a}$$

$$\bar{\boldsymbol{c}}_{\sim\mathrm{eb}} = \boldsymbol{c}_{\sim\mathrm{eb}} = \text{Arbitrary}. \tag{22b}$$

Likewise, letting $\bar{\boldsymbol{d}} = \boldsymbol{T}\boldsymbol{d}$, then, in view of Equation (19),

$$\bar{\boldsymbol{d}}_{\text{eb}} = \hat{\boldsymbol{U}}_{\text{eb}}, \qquad \bar{\boldsymbol{d}}_{\sim\text{eb}} = \boldsymbol{d}_{\sim\text{eb}}, \tag{23}$$

which relates the elements of $\bar{\boldsymbol{d}}_{\text{eb}}$ to the prescribed function $g_k(\boldsymbol{x})$, as defined in Equation (10). Following the procedure given by Wagner and Liu [2000],

$$\begin{bmatrix} \bar{\boldsymbol{c}}_{\text{eb}}^T & \bar{\boldsymbol{c}}_{\sim\text{eb}}^T \end{bmatrix} \left(\begin{bmatrix} \bar{\boldsymbol{K}}_{\text{eb,eb}} & \bar{\boldsymbol{K}}_{\text{eb,}\sim\text{eb}} \\ \bar{\boldsymbol{K}}_{\sim\text{eb,eb}} & \bar{\boldsymbol{K}}_{\sim\text{eb,}\sim\text{eb}} \end{bmatrix} \begin{bmatrix} \bar{\boldsymbol{d}}_{\text{eb}} \\ \bar{\boldsymbol{d}}_{\sim\text{eb}} \end{bmatrix} - \begin{bmatrix} \bar{\boldsymbol{f}}_{\text{eb}} \\ \bar{\boldsymbol{f}}_{\sim\text{eb}} \end{bmatrix} \right) = 0,$$

where

$$\bar{\boldsymbol{K}} = (\boldsymbol{T}^{-1})^T \boldsymbol{K} \boldsymbol{T}^{-1}, \qquad \bar{\boldsymbol{f}} = (\boldsymbol{T}^{-1})^T \boldsymbol{f},$$

and, using Equation (22) and Equation (23), we have

$$\bar{\boldsymbol{K}}_{\sim\text{eb,}\sim\text{eb}}\, \boldsymbol{d}_{\sim\text{eb}} = \bar{\boldsymbol{f}}_{\sim\text{eb}} - \bar{\boldsymbol{K}}_{\sim\text{eb,eb}} \hat{\boldsymbol{U}}_{\text{eb}}.$$

This equation can be readily solved for $\boldsymbol{d}_{\sim\text{eb}}$.

5. Kirchhoff plate

Consider a symmetric laminated composite plate on an elastic foundation of varying stiffness $k_f(x_1, x_2)$, as shown in Figure 4. The boundary conditions and the transverse applied loading $q(x_1, x_2)$ are arbitrary. The plate is also subjected to edge forces N_{ij}, $i, j = 1, 2$. According to the classical plate theory known as Kirchhoff theory, the governing partial differential equation associated with the deflection u_3 becomes [Reddy 1984]

$$(-N_{11}u_{3,1} + N_{12}u_{3,2})_{,1} + (-N_{22}u_{3,2} + N_{12}u_{3,1})_{,2} + M_{11,11} + M_{22,22} + 2M_{12,12} + k_f u_3 = q, \tag{24}$$

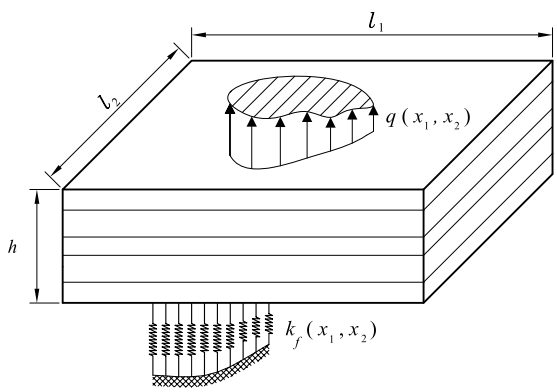

Figure 4. Schematic of a rectangular laminated composite plate with arbitrary loading and boundary conditions.

and the admissible boundary conditions for the present experiments consist of

$$\text{on } x_1 = 0,\ l_1 : \begin{cases} \text{either } -N_{11}u_{3,1} + N_{12}u_{3,2} + M_{11,1} + 2M_{12,2} = 0 & \text{or } u_3 \text{ specified,} \\ \text{either } \quad M_{11} = 0 & \text{or } u_{3,1} \text{ specified,} \end{cases}$$

$$\text{on } x_2 = 0,\ l_2 : \begin{cases} \text{either } -N_{22}u_{3,2} + N_{12}u_{3,1} + M_{22,2} + 2M_{12,1} = 0 & \text{or } u_3 \text{ specified,} \\ \text{either } \quad M_{22} = 0 & \text{or } u_{3,2} \text{ specified,} \end{cases} \tag{25}$$

at the corners: either $M_{12} = 0$ or u_3 specified.

In relations (24) and (25),

$$\begin{bmatrix} M_{11} \\ M_{22} \\ M_{12} \end{bmatrix} = \begin{bmatrix} D_{11} & D_{12} & 0 \\ D_{12} & D_{22} & 0 \\ 0 & 0 & D_{66} \end{bmatrix} \begin{bmatrix} u_{3,11} \\ u_{3,22} \\ 2u_{3,12} \end{bmatrix}, \tag{26}$$

where the D_{ij} are called the bending stiffnesses; see [Reddy 1997] for details. For a single isotropic layer with Young's modulus E and Poisson ratio ν, the D_{ij} become

$$D_{11} = D_{22} = D, \qquad D_{12} = \nu D, \qquad D_{66} = \frac{1-\nu}{2} D, \tag{27}$$

in which $D = Eh^3/(12 - 12\nu^2)$ is called the flexural rigidity of the plate.

The discretized weak form of Equation (24), employing the shape functions for two-dimensional space, $\boldsymbol{\psi}(x_1, x_2)$, yields

$$\begin{aligned} &\boldsymbol{c}^T \boldsymbol{r} = 0, \\ &\boldsymbol{r} = \boldsymbol{K}\boldsymbol{d} - \boldsymbol{f}, \\ &\boldsymbol{K} = \int_0^{l_2} \int_0^{l_1} dx_1\, dx_2 \Big[N_{11}\boldsymbol{\psi}_{,1}^T\boldsymbol{\psi}_{,1} + N_{22}\boldsymbol{\psi}_{,2}^T\boldsymbol{\psi}_{,2} + N_{12}(\boldsymbol{\psi}_{,1}^T\boldsymbol{\psi}_{,2} + \boldsymbol{\psi}_{,2}^T\boldsymbol{\psi}_{,1}) \\ &\qquad + D_{11}\boldsymbol{\psi}_{,11}^T\boldsymbol{\psi}_{,11} + D_{22}\boldsymbol{\psi}_{,22}^T\boldsymbol{\psi}_{,22} + 4D_{66}\boldsymbol{\psi}_{,12}^T\boldsymbol{\psi}_{,12} \\ &\qquad + D_{12}\big(\boldsymbol{\psi}_{,22}^T\boldsymbol{\psi}_{,11} + \boldsymbol{\psi}_{,11}^T\boldsymbol{\psi}_{,22}\big) + k_f\boldsymbol{\psi}^T\boldsymbol{\psi} \Big], \\ &\boldsymbol{f} = \int_0^{l_2} \int_0^{l_1} q\boldsymbol{\psi}^T dx_1 dx_2. \end{aligned} \tag{28}$$

For studying the stability of the plate, we put $\boldsymbol{f} = \boldsymbol{0}$. This and Equation (28) give

$$\boldsymbol{c}^T(\boldsymbol{K}^L - \lambda \boldsymbol{K}^G)\boldsymbol{d} = 0, \tag{29}$$

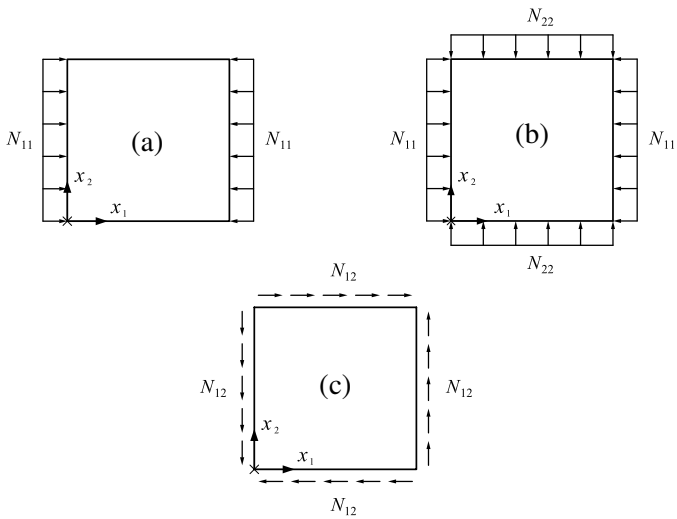

Figure 5. Midplane of an isotropic plate subjected to (a) uniaxial compression, (b) biaxial compression, and (c) uniform shear.

where

$$\begin{aligned}
\boldsymbol{K}^{L} &= \int_0^{l_2}\int_0^{l_1} dx_1\,dx_2\Big[D_{11}\boldsymbol{\psi}_{,11}^{T}\boldsymbol{\psi}_{,11} + D_{22}\boldsymbol{\psi}_{,22}^{T}\boldsymbol{\psi}_{,22} + 4D_{66}\boldsymbol{\psi}_{,12}^{T}\boldsymbol{\psi}_{,12} \\
&\qquad + D_{12}\big(\boldsymbol{\psi}_{,22}^{T}\boldsymbol{\psi}_{,11} + \boldsymbol{\psi}_{,11}^{T}\boldsymbol{\psi}_{,22}\big) + k_f\boldsymbol{\psi}^{T}\boldsymbol{\psi}\Big], \\
\boldsymbol{K}^{G} &= \int_0^{l_2}\int_0^{l_1} dx_1\,dx_2\Big[\hat{N}_{11}\boldsymbol{\psi}_{,1}^{T}\boldsymbol{\psi}_{,1} + \hat{N}_{22}\boldsymbol{\psi}_{,2}^{T}\boldsymbol{\psi}_{,2} + \hat{N}_{12}(\boldsymbol{\psi}_{,1}^{T}\boldsymbol{\psi}_{,2} + \boldsymbol{\psi}_{,2}^{T}\boldsymbol{\psi}_{,1})\Big], \\
\lambda &= -\frac{N_{11}}{\hat{N}_{11}} = -\frac{N_{22}}{\hat{N}_{22}} = -\frac{N_{12}}{\hat{N}_{12}}.
\end{aligned} \tag{30}$$

Equation (29) is an eigenvalue problem, in which λ is the eigenvalue corresponding to the critical load and $\boldsymbol{d}$ is the eigenvector associated with the DOF. The eigenvector is normalized to have Euclidean length one. Therefore, the displacement obtained from Equation (13a) is dimensionless.

Standard Gaussian quadratures carry out the numerical integrations in Equations (28) and (30). For this, a background mesh is needed, and we set the nodes of the background mesh to coincide with the meshless particles and compute a 4×4 quadrature in each cell.

6. Numerical experiments

In this section, we demonstrate the applicability and efficacy of the proposed method in treating various boundary conditions encountered in plate problems. We compare the accuracy of the results with analytical solutions, whenever they are available. We investigate the method's advantages over conventional meshfree methods by considering several examples.

6.1. ***GRKPM versus RKPM.*** Consider a clamped square plate with elastic modulus and Poisson ratio of $E = 2 \times 10^9$ N/m^2 and $\nu = 0.3$. For each of the loading conditions in Figure 5, we solve for the critical load and the corresponding mode shape.

The expression for the critical load is

$$N_{ij} = \lambda \frac{\pi^2 D}{l^2}, \ i, j = 1, 2,$$

in which the analytical values for λ [Timoshenko and Gere 1961] are

$$\lambda_{\text{Anal.}} = \begin{cases} 10.07, & \text{Uniform uniaxial compression,} \\ 5.30, & \text{Uniform biaxial compression,} \\ 14.71, & \text{Uniform shear.} \end{cases} \tag{31}$$

For numerical calculations, we set the plate dimensions to $l = 5$ m and $h = 0.05$ m, distribute the particles distributed uniformly in the x_1 and x_2-directions, and employ the linear correction function. We set the dilation parameter in the x_1 and x_2-directions to 1.8 times the corresponding interparticle distance Δy_i.

Each loading condition in Figure 5 leads to an eigenvalue problem, with analytical solutions given in Equation (31). Numerically, we solve each by RKPM combined with the penalty method, and also by our GRKPM. For RKPM, Table 1 displays the required CPU time and the percent error for selected numbers of particles; Table 2 does the same for GRKPM.

The GRKPM gives fair accuracy in all cases, even for relatively small numbers of particles. In the very worst case — in shear loading with a 5×5 distribution of particles — the error is only 5.8%. In comparison, the best result (in biaxial loading) for conventional RKPM has 22.5% error, and that was for a considerably larger 16×16 number of particles. In that case, the GRKPM already gives an error of 0.0% (to two-digit accuracy) with the smallest 5×5 number of particles. The GRKPM does cost more in CPU time for a fixed number of particles, but, because it achieves better accuracy using smaller number of particles, the GRKPM significantly outperforms RKPM at fixed CPU time.

We have computed the critical mode shapes using our method with an 8×8 distribution of particles; these are shown in Figure 6. Note that the symmetric loading conditions shown in Figure 5a and b allow us to consider only one-quarter of the plate. For the unsymmetric loading conditions of Figure 5c, the entire plate must be modeled.

Particles		11×11		13×13		14×14		16×16	
Loading	$\lambda_{\text{Anal.}}$	Time (s)	Error (%)	Time (s)	Error (%)	Time (s)	Error (%)	Time (s)	Error (%)
Figure 5a	10.07	2.3	34.5	3.5	28.8	4.5	26.7	7.6	23.4
Figure 5b	5.30	2.3	33.0	3.6	27.5	4.5	25.7	7.8	22.5
Figure 5c	14.71	2.6	39.0	3.8	31.3	4.8	28.7	7.8	24.7

Table 1. CPU time and percent error of the buckling parameters using RKPM, with $\boldsymbol{a} = 1.8\Delta \boldsymbol{y}$.

Particles		5×5		6×6		7×7		8×8	
Loading	$\lambda_{\text{Anal.}}$	Time (s)	Error (%)	Time (s)	Error (%)	Time (s)	Error (%)	Time (s)	Error (%)
Figure 5a	10.07	2.4	0.2	3.4	0.1	4.8	0.1	7.2	0.0
Figure 5b	5.30	2.4	0.0	3.4	0.0	4.9	0.0	7.3	0.0
Figure 5c	14.71	2.4	5.8	3.3	1.6	4.8	1.3	7.1	1.1

Table 2. CPU time and percent error of the buckling parameters using GRKPM, with $\boldsymbol{a} = 1.8\Delta \boldsymbol{y}$.

6.2. ***GRKPM and effects of the dilation parameter.*** Zhao et al.[2003; 2004] and Liew et al. 2005 have investigated how the dilation parameter and particle distribution influence the convergence of meshless approaches such as RKPM; these studies have proved useful. This section performs such studies for GRKPM. To this end, we consider the clamped square plate defined in the previous section. The problem is solved with uniform distributions of particles and various values for the ratio of the dilation parameter to the interparticle distance, $a_i/\Delta y_i = 1.75, 2.00, 2.25, 2.5$. For uniaxial and biaxial compression, only one quarter of the plate is modeled, due to symmetry, and the region of the plate is $[0, 2.5]^2$. The number of particles along each edge varies from 5×5 to 9×9. Figure 7 shows how the buckling factor λ varies with the number of particles along each edge for uniaxial and biaxial cases. This figure show monotonic convergence and remarkably accurate results for all the dilation parameters. The most accurate outcomes obtain when $a_i/\Delta y_i = 1.75$. For larger dilation parameters, the results are less accurate, but the accuracy quickly approaches that of smaller parameters as the number of particles increases.

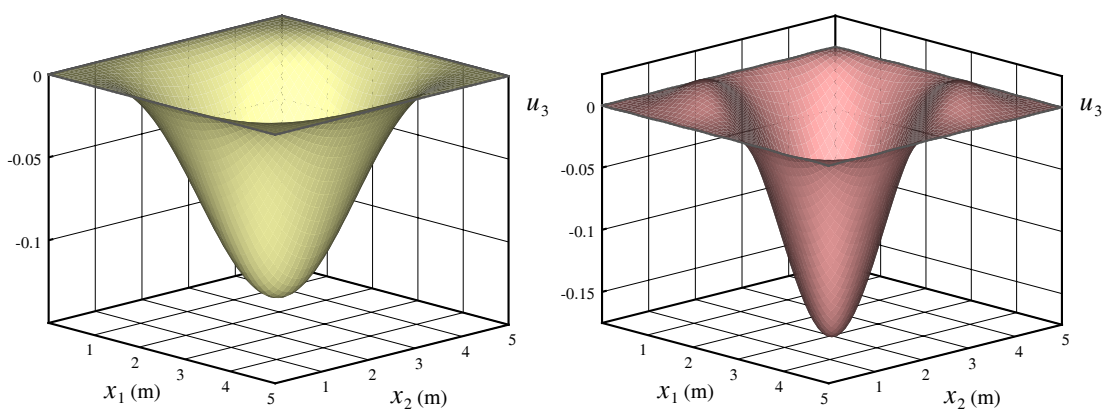

Figure 6. Critical buckling mode shapes of the isotropic square plate of Figure 5a, b, and, at right, from the uniform shear of the clamped square isotropic plate. At left, the plate is under uniaxial/biaxial compression; at right it is under uniform shear. See Figure 5.

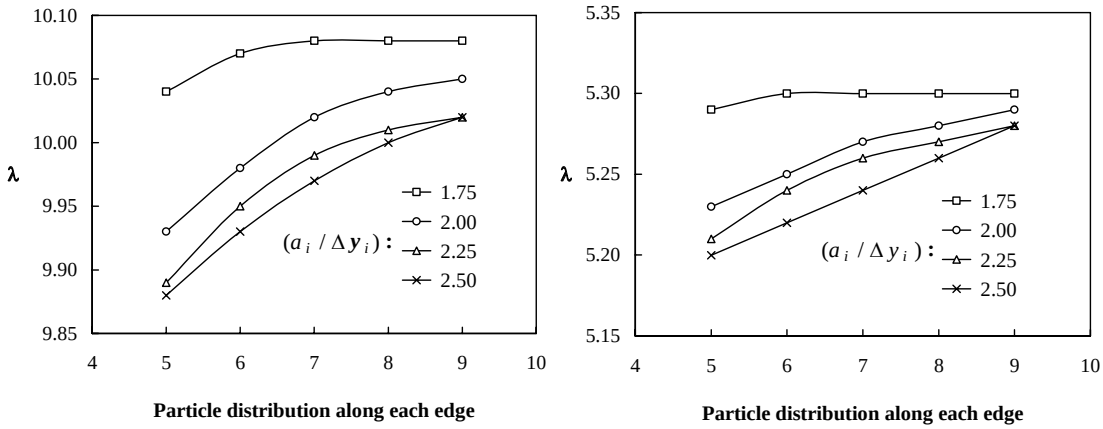

Figure 7. Convergence of the buckling parameter λ with increasing number of particles along each edge and for various dilation parameters. At left, the clamped square plate is under uniaxial compression; at right, it is under biaxial compression. See Section 6.1.

For the uniform shear test, we model the entire plate, and the region of analysis is $[0, 5]^2$. We consider various uniform distributions of paricles ranging from 6×6 to 10×10. (The number of particles varies from 36 to 100.) Figure 8 displays how the buckling factor λ varies with the number of particles along each edge. The results converge monotonically and, for any distribution of particles, are always closest when $a_i/\Delta y_i = 1.75$. Because we reached the same conclusion before in uniform uniaxial and biaxial compression tests, we adopt the value $a_i/\Delta y_i = 1.75$ for further experiments.

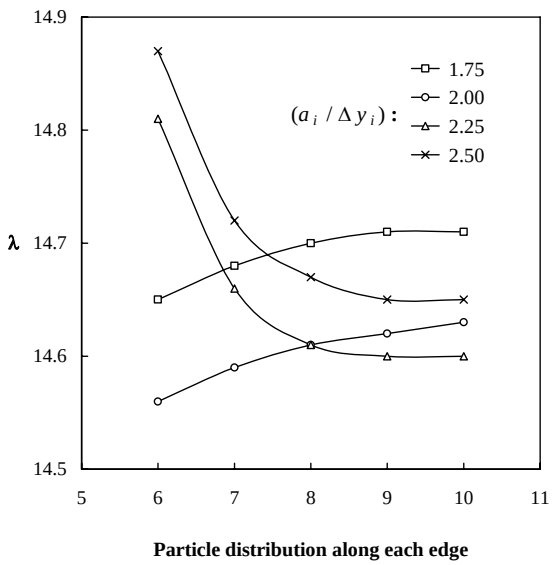

Figure 8. Convergence of the buckling parameter λ with increasing number of particles along each edge and for various dilation parameters. The clamped square plate is under uniform shear. See Section 6.1.

6.3. ***GRKPM versus EFGM.*** Consider a thin rectangular plate of thickness h and dimensions l_1 and l_2 in x_1 and x_2. To compare the performance of EFGM and GRKPM, we compute the critical buckling load for various aspect ratios l_1/l_2 and different types of boundary conditions by both methods. The edge load is applied in the x_1-direction, as shown in Figure 5a. In the numerical calculations, we use $l_2 = 10\,\text{m}$ and $h = 0.06\,\text{m}$ and assume the plate to be isotropic with $E = 2.45 \times 10^6\,\text{N/m}^2$ and $\nu = 0.23$. The buckling load N and the buckling factor λ are related as

$$N = \lambda \frac{\pi^2 D}{l_2^2}.$$

Table 3 tabulates the analytical [Timoshenko and Gere 1961] and computed values of λ for simply supported boundary conditions along all the edges and for different aspect ratios l_1/l_2. The numerical calculations used a 13×13 uniform distribution of particles. The results of EFGM in conjunction with the penalty method are cited from [Liu 2003]. There, Liu [2003] notes that the optimal dilation parameter is somewhere between 3.5 to 3.9 times the interparticle distance. Accordingly, for each l_1/l_2, the dilation parameter is tuned within this rather tight range [Liu 2003]. Moreover, this particular EFGM uses the second-order base function instead of the first. In contrast, the GRKPM here employs the first-order base function. Moreover, for each l_1/l_2, we examine two rather different dilation parameters, $a_i = 1.72\Delta y_i$ and $a_i = 3.5\Delta y_i$. Even though these dilation parameters differ by more than a factor of two, the results in either case are much better than those given by the EFGM with restricted dilation parameters. We conclude that the GRKPM is somewhat indifferent to the dilation parameter.

Method	Analytical	EFGM	GRKPM	
$a_i/\Delta y_i$	–	3.5–3.9	1.72	3.5
I_1/I_2	λ	Percent error		
0.20	27.00	0.33	0.15	0.15
0.30	13.20	0.15	0.00	0.00
0.40	8.41	0.12	0.00	0.00
0.50	6.25	0.00	0.00	−0.16
0.60	5.14	−0.19	0.00	0.00
0.70	4.53	0.00	0.00	0.00
0.80	4.20	0.00	0.00	0.00
0.90	4.04	0.00	0.00	0.00
1.00	4.00	1.00	0.00	0.00
1.10	4.04	0.25	0.00	0.00
1.20	4.13	0.00	0.00	0.00
1.30	4.28	0.00	0.00	0.00
1.40	4.47	0.22	0.00	−0.45

Table 3. Buckling factor for the simply supported rectangular plate.

Method	Analytical	EFGM	GRKPM	
$a_i/\Delta y_i$	–	3.5–3.9	1.72	3.5
I_1/I_2	λ	Percent error		
0.4	9.44	0.42	0.00	0.00
0.5	7.69	0.39	0.00	0.00
0.6	7.05	0.85	0.00	0.00
0.7	7.00	0.71	−0.14	0.00
0.8	7.29	1.23	0.14	0.14
0.9	7.83	1.66	0.26	0.26
1.0	7.69	1.04	0.00	0.00

Table 4. Buckling factor for the rectangular plate with simply supported, and clamped edges.

Table 4 displays the analytical [Timoshenko and Gere 1961] and computed values of λ when the edges $x_1 = 0, l_1$ are simply supported and the edges $x_2 = 0, l_2$ are fixed. All the other conditions and parameters are kept from the previous case. Again, for a given particle distribution, GRKPM allows more flexibility in choosing the dilation parameter and yields more accurate results. As before, EFGM uses the second-order base function, while the GRKPM uses first-order base function.

6.4. ***GRKPM and various types of boundary conditions.*** Figure 9 shows a schematic of a cross-ply laminate (90/0/90). The mark $\times$ locates the origin of the Cartesian coordinate system. The edges $x_2 = 0, l$ are assumed to be simply supported and under a uniform compressive load along the x_2-direction. For the other two edges, $x_1 = 0, l$, we consider various combinations of free, simply supported, and clamped boundary conditions, denoted respectively by F, S, and C. We put $l = 5\,\text{m}$ and the thickness of each lamina to 0.05 m. We assume that each lamina is made of carbon-epoxy with the material properties $E_1 = 40E_2$, $G_{12} = 0.6E_2$ and $\nu_{12} = 0.25$.

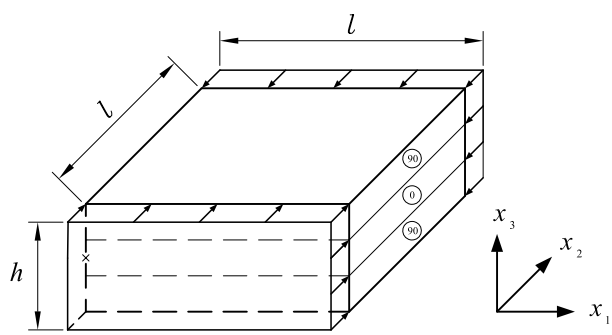

Figure 9. Square cross-ply laminate (90/0/90) subjected to uniform compressive load along the x_2 axis.

	Levy	GRKPM					
BC	λ	Particles	λ	% Err.	Particles	λ	% Err.
FF	31.76	5×5	31.41	-1.10	9×9	31.66	-0.33
FS	32.34	9×5	31.85	-1.49	17×9	32.22	-0.37
FC	32.81	9×5	32.18	-1.92	17×9	32.65	-0.48
SS	36.16	5×5	35.97	-0.52	9×9	36.12	-0.11
SC	39.43	9×5	39.36	-0.17	17×9	39.41	-0.05
CC	45.06	5×5	44.78	-0.63	9×9	45.02	-0.10

Table 5. Buckling factor for the cross-ply (90/0/90) square plate with mixed boundary conditions.

For this problem, the buckling load N and the buckling factor λ are related as

$$N = \lambda \frac{l^2}{E_2 h^3}. \tag{32}$$

The Levy method [Reddy 1997] is used to calculate the analytical values of λ. In our GRKPM, we find λ using a uniform distribution of particles and a dilation parameter of 1.75 times the interparticle distance. For SS, CC, and FF boundary conditions, we model only one quarter of the plate, whereas, for FS, FC, and SC conditions, we model half the plate. Table 5 compares the results with the analytical solutions. The BVPs associated with FF, SS and CC boundary conditions are solved for 5×5 and 9×9 particles, whereas, for the cases FS, FC and SC, we use 9×5 and 17×9 particles. Table 5 shows that the GRKPM yields satisfactory results even with the smallest number of particles. The maximum error obtains with the FC boundary conditions; the error is -1.92% for 9×5 particles and -0.48% for 17×9 particles. The SC boundary conditions, on the other hand, minimize the error; it is -0.17% for 9×5 and -0.05% for 17×9 particles. Table 5 shows clearly that the results improve as the number of particles increases.

6.5. ***Symmetric laminated composite plate under the most general conditions via GRKPM.*** To implement the proposed approach, we have developed a powerful program we call ALCP-GRKPM (analysis of laminated composite plates via GRKPM) for analyzing symmetric laminated composite plates with arbitrary loading and boundary conditions. For example, consider the laminated composite $(70/-20)_S$ shown in Figure 10, in which the thicknesses of the layers are $(0.02\,\text{m}/0.03\,\text{m})_S$. Each lamina is made of carbon-epoxy (AS4/3501-6) with $E_1 = 148\,\text{GPa}$, $E_2 = 10.5\,\text{GPa}$, $G_{12} = G_{13} = 5.61\,\text{GPa}$, $G_{23} = 3.17\,\text{GPa}$, $\nu_{12} = \nu_{13} = 0.3$ and $\nu_{23} = 0.59$. The edge $x_2 = 0$ is free and the remaining edges are clamped. A roller type support is placed in the middle of the plate, and part of the plate is placed on elastic foundation. We solve this set problem for two different cases: (1) uniform spring constant and distributed load; and (2) variable spring constant and distributed load. For both cases, a concentrated load of $P = 50\,\text{kN}$ is applied at the location marked $\odot$ in Figure 10. In this computation, we intend to find the location and value of the maximum deflection. We use 9×5, 17×9, 33×17, and 65×33 uniformly distributed particles. We set the dilation parameter equal to 1.75 times the interparticle distance.

Case 1: Uniform spring constant and uniformly distributed load. In this case the spring constant and distributed load are $k_f = 10^5\,\text{kN/m}^3$ and $q = 80\,\text{kN/m}^2$. For reference, we analyze the problem by

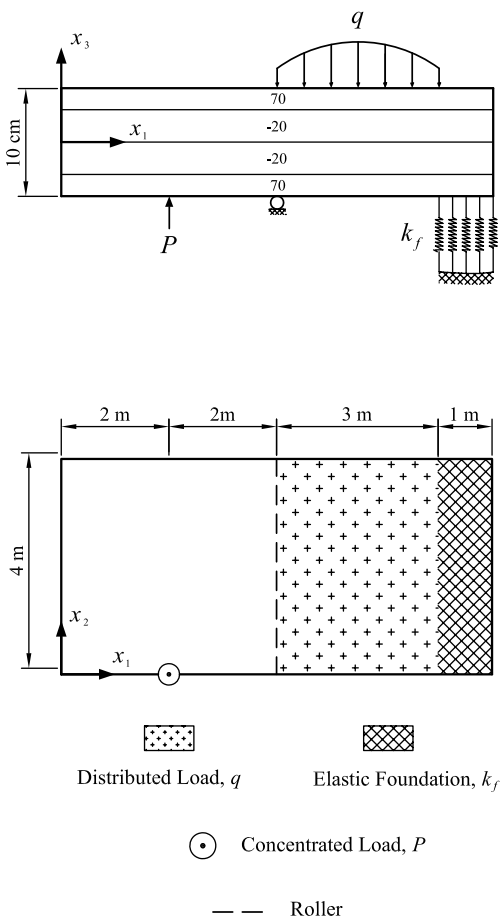

Figure 10. An example of a rectangular symmetric laminate $(70/-20)_s$ under a set of complex loadings and boundary conditions.

Method	Particles	$(u_3)_{\max}$ (cm)	x_1 (m)	x_2 (m)
GRKPM	9×5	-2.002	5.6250	0.000
	17×9	-2.003	5.6250	0.000
	33×17	-2.005	5.6250	0.000
	65×33	-2.006	5.6250	0.000
ANSYS	65×33	-2.072	5.6250	0.000

Table 6. Location and value of the maximum deflection for the plate shown in Figure 10 with a uniform elastic constant and a uniformly distributed load.

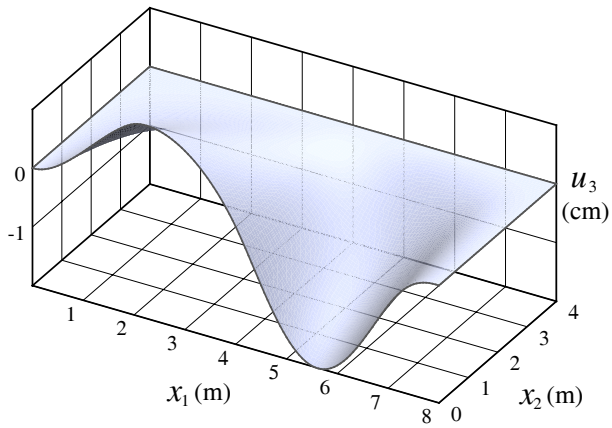

Figure 11. ALCP-GRKPM result for the deflection corresponding to the example shown in Figure 10 with uniform elastic constant and a uniformly distributed load.

ANSYS using 65×33 uniformly spaced nodes. In employing ANSYS, we use the 8-node 'Shell 99' element. Appendix A gives its interpolation functions, assumptions, and restrictions. At each node, the element has three displacement and three rotational DOF. Because of this, the DOF per node in ANSYS is twice the DOF per particle GRKPM. Table 6 shows the maximum deflection of the plate and where it occurs. GRKPM with 45 particles already gives a satisfactory result, and making more particles only affects the third decimal digit in the maximum deflection. The small discrepancy between the results of ANSYS and GRKPM for the maximum deflection arises because ANSYS applies the first-order shear deformation laminated plate theory (FSDT) [Reddy 1997] which considers shear deflections, whereas we use the classical plate theory which disregards these deflections. To suppress the shear deflections in FSDT, the lateral shear moduli G_{13} and G_{23} should be assigned significantly larger than G_{12}. Ansys [1997] recommends taking $G_{13} = G_{23} = 1000G_{12}$. By doing so, the computed maximum deflection equals 2.006, which agrees with the GRKPM result to within three decimal places. The deflection, $u_3(x_1, x_2)$, is computed by GRKPM with 65×33 particles, and its variation is shown in Figure 11.

Case 2: Variable spring constant and variably distributed load. The program ALCP-GRKPM can accept $q(x_1)$ and $k_f(x_1, x_2)$ as functions. For example, consider the plate shown in Figure 10 with the spring constant and distributed load assigned to vary as

$$k_f = \frac{10^6}{x_1 + x_2}\,\text{kN/m}^3, \qquad q = 55(x_1 - 4)(x_1 - 7)\,\text{kN/m}^2.$$

Table 7 gives the corresponding results for 9×5, 17×9, 33×17 and 65×33 uniformly distributed particles. As in the previous example, increasing the number of particles only affects the third decimal digit in the maximum displacement.

7. Conclusions

We have demonstrated that our method is robust by considering plate boundary value problems. The results demonstrate that the method succeeds in treating different kinds of EBCs including those with

Method	Particles	$(u_3)_{\max}$ (cm)	x_1 (m)	x_2 (m)
GRKPM	9×5	-2.363	5.5625	0.000
	17×9	-2.366	5.6250	0.000
	33×17	-2.368	5.6250	0.000
	65×33	-2.370	5.6250	0.000

Table 7. Location and value of the maximum deflection for the plate shown in Figure 10 for variable elastic constant and a variably distributed load.

derivatives of the field function. The examples compute buckling load and analyze deflection under various types of loading and support, including elastic foundation with variable stiffness as explored in Section 6.5.

In the example of Section 6.1, comparing the performance of GRKPM and conventional RKPM reveals that using GRKPM with much smaller numbers of particles leads to results of excellent accuracy. In Section 6.2, from studying how the number of particles and the dilation parameter affect the performance of GRKPM, we conclude the GRKPM converges well as the number of particles increases. In Section 6.3, we conclude that for GRKPM the base function of order one suffices for obtaining better accuracy than from EFGM with the second-order base function. Moreover, for the cross-ply laminate with various types of EBCs considered in Section 6.4, the GRKPM solution converges rapidly with growing number of particles.

The presently formulated GRKPM achieves high performance because it expands the degrees of freedoms to include slopes and because it enforces EBCs by generalizing the corrected collocation method. Hence, the advantages become more pronounced for plates clamped at the boundaries. Given its so-far excellent features, GRKPM may hold promise for other problems of engineering science.

Appendix A

'Shell 99' is an 8-node quadrilateral element in 3-dimensions with rotational DOF and shear deflection [Ansys 1997]. It is suitable for laminate composites and can accept up to 100 different layers. This element is discussed by Yunus et al. [1989]. A planner view of this element is given in Figure 12.

Let define the shape functions for each node as

$$\psi_1 = \frac{(1-s)(1-t)(-s-t-1)}{4}, \qquad \psi_2 = \frac{(1+s)(1-t)(s-t-1)}{4},$$
$$\psi_3 = \frac{(1+s)(1+t)(s+t-1)}{4}, \qquad \psi_4 = \frac{(1-s)(1+t)(-s+t-1)}{4},$$
$$\psi_5 = \frac{(1-s^2)(1-t)}{2}, \qquad \psi_6 = \frac{(1+s)(1-t^2)}{2},$$
$$\psi_7 = \frac{(1-s^2)(1+t)}{2}, \qquad \psi_8 = \frac{(1-s)(1-t^2)}{2}.$$

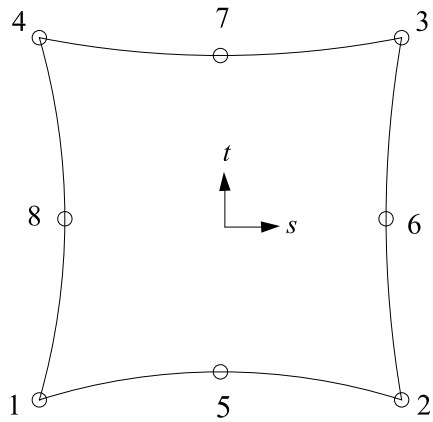

Figure 12. A planner view of the 'Shell 99' element used by ANSYS.

Subsequently, the interpolation functions are

$$\begin{bmatrix} u_1 \\ u_2 \\ u_3 \end{bmatrix} = \sum_{i=1}^{8} \psi_i \begin{bmatrix} u_1^i \\ u_2^i \\ u_3^i \end{bmatrix} + \sum_{i=1}^{8} \psi_i \frac{r t_i}{2} \begin{bmatrix} \hat{a}_1^i & \hat{b}_1^i \\ \hat{a}_2^i & \hat{b}_2^i \\ \hat{a}_3^i & \hat{b}_3^i \end{bmatrix} \begin{bmatrix} \theta_1^i \\ \theta_2^i \end{bmatrix}, \tag{A.1}$$

where u_1^i, u_2^i, and u_3^i are motions of node i, r is the coordinate along the thickness, and t_i is the thickness at node i. $\hat{\boldsymbol{a}}$ is the unit vector in the s direction and $\hat{\boldsymbol{b}}$ is the unit vector in the plane of element and normal to $\hat{\boldsymbol{a}}$. θ_1^i and θ_2^i are the rotations of node i about vector $\hat{\boldsymbol{a}}$ and $\hat{\boldsymbol{b}}$, respectively. An interesting observation is made by comparing the interpolation functions (A.1) with those of GRKPM given by Equation (7). The latter gives four different types of shape functions for the displacements and rotations of each node, whereas Equation (A.1) gives only one.

There are some assumptions and restrictions for this element:

- Normals to the center plane are assumed to remain straight after deformation, but not necessarily normal to the center plane.
- Each pair of integration points in the r direction is assumed to have the same material orientation.
- There is no significant stiffness associated with rotation about the element r axis. However, a nominal value of stiffness is present to prevent free rotation at the node.

Acknowledgement

This work was in part supported by the center of excellence in structures and earthquake engineering at Sharif University of Technology.

References

[Ansys 1997] Ansys, "ANSYS 5.4 Documentation", Technical report, ANSYS Incorporated, 1997.

[Atluri et al. 1999] S. N. Atluri, J. Y. Cho, and H.-G. Kim, "Analysis of thin beams, using the meshless local Petrov–Galerkin method, with generalized moving least squares interpolations", *Comput. Mech.* **24**:5 (1999), 334–347.

[Belytschko et al. 1994a] T. Belytschko, L. Gu, and Y. Y. Lu, "Fracture and crack growth by element free Galerkin methods", *Model. Simul. Mater. Sc.* **2**:3A (1994), 519–534.

[Belytschko et al. 1994b] T. Belytschko, Y. Y. Lu, and L. Gu, "Element-free Galerkin methods", *Int. J. Numer. Meth. Eng.* **37**:2 (1994), 229–256.

[Chen et al. 1996] J. S. Chen, C. Pan, C. T. Wu, and W. K. Liu, "Reproducing kernel particle methods for large deformation analysis of non-linear structures", *Comput. Method. Appl. M.* **139**:1-4 (1996), 195–227.

[Donning and Liu 1998] B. M. Donning and W. K. Liu, "Meshless methods for shear-deformable beams and plates", *Comput. Method. Appl. M.* **152**:1-2 (1998), 47–71.

[Hashemian 2000] A. Hashemian, "A study of Columns' buckling loads and modes by meshfree methods", Master's Thesis, Sharif University of Technology, Tehran, 2000.

[Krongauz and Belytschko 1996] Y. Krongauz and T. Belytschko, "Enforcement of essential boundary conditions in meshless approximations using finite elements", *Comput. Method. Appl. M.* **131**:1-2 (1996), 133–145.

[Lam et al. 2006] K. Y. Lam, H. Li, Y. K. Yew, and T. Y. Ng, "Development of the meshless Hermite-Cloud method for structural mechanics applications", *Int. J. Mech. Sci.* **48**:4 (2006), 440–450.

[Lancaster and Salkauskas 1981] P. Lancaster and K. Salkauskas, "Surfaces generated by moving least squares methods", *Math. Comput.* **37**:155 (1981), 141–158.

[Li and Liu 2002] S. Li and W. K. Liu, "Meshfree and particle methods and their applications", *Appl. Mech. Rev. (Trans. ASME)* **55**:1 (2002), 1–34.

[Li et al. 2003] H. Li, T. Y. Ng, J. Q. Cheng, and K. Y. Lam, "Hermite-Cloud: a novel true meshless method", *Comput. Mech.* **33**:1 (2003), 30–41.

[Li et al. 2004] S. Li, H. Lu, W. Han, W. K. Liu, and D. C. Simkins, "Reproducing kernel element method, II: globally conforming I^m/C^n hierarchies", *Comput. Method. Appl. M.* **193**:12-14 (2004), 953–987.

[Liew et al. 2005] K. M. Liew, T. Y. Ng, and X. Zhao, "Free vibration analysis of conical shells via the element-free kp-Ritz method", *J. Sound Vib.* **281**:3-5 (2005), 627–645.

[Liu 2003] G. R. Liu, *Mesh free methods: moving beyond the finite element method*, CRC Press, Boca Raton, FL, 2003.

[Liu et al. 1995] W. K. Liu, S. Jun, and Y. F. Zhang, "Reproducing kernel particle methods", *Int. J. Numer. Meth. Fl.* **20**:8-9 (1995), 1081–1106.

[Liu et al. 1996a] W. K. Liu, Y. J. Chen, R. A. Uras, and C. T. Chang, "Generalized multiple scale reproducing kernel particle methods", *Comput. Method. Appl. M.* **139**:1-4 (1996), 91–157.

[Liu et al. 1996b] W. K. Liu, S. Jun, J. S. Chen, T. Belytschko, C. Pan, R. A. Uras, and C. T. Chang, "Overview and applications of the reproducing kernel particle methods", *Arch. Comput. Method E* **3** (1996), 3–80.

[Liu et al. 1997] W. K. Liu, R. A. Uras, and Y. Chen, "Enrichment of the finite element method with reproducing kernel particle method", *J. Appl. Mech.* (*Trans. ASME*) **64** (1997), 861–870.

[Liu et al. 2004] W. K. Liu, W. Han, H. Lu, S. Li, and J. Cao, "Reproducing kernel element method, I: theoretical formulation", *Comput. Method. Appl. M.* **193**:12-14 (2004), 933–951.

[Lu et al. 1994] Y. Y. Lu, T. Belytschko, and L. Gu, "A new implementation of the element free Galerkin method", *Comput. Method. Appl. M.* **113**:3-4 (1994), 397–414.

[Lucy 1977] L. B. Lucy, "A numerical approach to the testing of the fission hypothesis", *The Astro. J.* **82** (1977), 1013–1024.

[Reddy 1984] J. N. Reddy, *Energy and variational methods in applied mechanics: with an introduction to the finite element method*, John Wiley & Sons, New York, 1984.

[Reddy 1997] J. N. Reddy, *Mechanics of laminated composite plates: theory and analysis*, CRC Press, Boca Raton, FL, 1997.

[Tiago and Leitão 2004] C. Tiago and V. M. A. Leitão, "Further developments on GMLS: plates on elastic foundation", pp. 1378–1383 in *Proceedings of the 2004 international conference on computational and experimental engineering and science* (Madeira, Portugal), edited by A. Tadeu and S. N. Atluri, Tech Science Press, 2004, Available at http://www.civil.ist.utl.pt/~ctf/docs/04b_madeira.pdf.

[Timoshenko and Gere 1961] S. P. Timoshenko and J. M. Gere, *Theory of elastic stability*, 2nd ed., McGraw-Hill, New York, 1961.

[Wagner and Liu 2000] G. J. Wagner and W. K. Liu, "Application of essential boundary conditions in mesh-free methods: a corrected collocation method", *Int. J. Numer. Meth. Eng.* **47**:8 (2000), 1367–1379.

[Yunus et al. 1989] S. M. Yunus, P. C. Kohnke, and S. Saigal, "An efficient through-thickness integration scheme in an unlimited layer doubly curved isoparametric composite shell element", *Int. J. Numer. Meth. Eng.* **28**:12 (1989), 2777–2793.

[Zhao et al. 2003] X. Zhao, K. M. Liew, and T. Y. Ng, "Vibration analysis of laminated composite cylindrical panels via a meshfree approach", *Int. J. Solids Struct.* **40**:1 (2003), 161–180.

[Zhao et al. 2004] X. Zhao, T. Y. Ng, and K. M. Liew, "Free vibration of two-side simply-supported laminated cylindrical panels via the mesh-free kp-Ritz method", *Int. J. Mech. Sci.* **46**:1 (2004), 123–142.

[Zhu and Atluri 1998] T. Zhu and S. N. Atluri, "A modified collocation method and a penalty formulation for enforcing the essential boundary conditions in the element free Galerkin method", *Comput. Mech.* **21**:3 (1998), 211–222.

Received 16 Oct 2006. Accepted 31 May 2007.

ALIREZA HASHEMIAN: al.hash@gmail.com
Center of Excellence in Structures and Earthquake Engineering, Department of Civil Engineering, Sharif University of Technology, P.O. Box 11365-9311, Tehran, Iran

HOSSEIN M. SHODJA: shodja@sharif.edu
Center of Excellence in Structures and Earthquake Engineering, Department of Civil Engineering, Sharif University of Technology, P.O. Box 11365-9311, Tehran, Iran